Visualizing dendritic characteristics of corticotropin-releasing hormone neurons at single-cell resolution in the whole mouse brain

Yu Wang[a,b], Pu Hu[a,b], Qinghong Shan[a,b], Chuan Huang[a,b], Zhaohuan Huang[a,b], Peng Chen[a,b], Anan Li[b,c], Hui Gong[b,c,*], and Jiang-Ning Zhou[a,b,*]

a. Chinese Academy of Science Key Laboratory of Brain Function and Diseases, School of Life Sciences, University of Science and Technology of China, Anhui, PR China;

b. Center for Excellence in Brain Science and Intelligence Technology, Chinese Academy of Sciences, Shanghai, 200031, China;

c. Britton Chance Center for Biomedical Photonics, Wuhan National Laboratory for Optoelectronics, MoE Key Laboratory for Biomedical Photonics, School of Engineering Sciences, Huazhong University of Science and Technology, Wuhan 430074, China.

* Hui Gong or Jiang-Ning Zhou.

Email: huigong@mail.hust.edu.cn or jnzhou@ustc.edu.cn

Abstract

Corticotropin-releasing hormone (CRH) is an important neuromodulator with wide distribution in the brain. Here, we screened the CRH-IRES-Cre;Ai32 mouse line to reveal the morphologies of individual CRH neurons throughout the mouse brain by using fluorescence micro-optical sectioning tomography (fMOST) system. Diverse dendritic morphologies and projection fibers were found in various brain regions. Reconstructions showed hypothalamic CRH neurons had the smallest somatic volumes and simplest dendritic branches, and CRH neurons in several regions shared a bipolar morphology. Further investigations in the medial prefrontal cortex unveiled somatic depth-dependent morphologies that exhibited three types of connections and CRH neurons in the anterior parvicellular area of hypothalamus had fewer and smaller Herring bodies whereas in the periventricular area had more and larger Herring bodies that were present within fibers projecting to the third ventricle. Our findings provide the most comprehensive intact morphologies of CRH neurons throughout the mouse brain that is currently available.

Introduction

Corticotropin-releasing hormone (CRH), a 41–amino acid peptide, is an important neuromodulator with wide distribution in the brain (Spiess et al., 1981). As a neuroendocrine hormone, CRH is abundantly expressed in hypothalamic paraventricular nucleus (PVN) neurons and plays a crucial role in the regulation of the hypothalamic-pituitary-adrenal (HPA) axis (Albeck et al., 1997; Mezey et al., 1984). CRH-expressing neurons are also broadly distributed in other brain regions, including the inferior olivary nucleus, Barrington's nucleus, pontine tegmentum, cerebral cortex, hippocampus, and central amygdala. Depending on the region-specific somatic locations, CRH neurons participate in various functional activities, such as learning memory, synaptic plasticity, food intake and drug addiction, as well as anxiety-like and depression-like behaviors (Gallopin et al., 2006; Miyata et al., 1999; Puder and Papka, 2001; Sasaki and Sato, 2013).

The anatomy of the brain CRH system has been studied in different mammalian species via immunohistochemistry and radioimmunoassays (Bassett and Foote, 1992;

Charlton et al., 1987; Cummings, 1989; Delville et al., 1992; Foote and Cha, 1988; Merchenthaler, 1984; Shu et al., 2015). However, data from these studies have mainly been acquired from histological imaging and through manual reconstruction and counting of labeled neurons, which is time-consuming, limits further systematic analysis, and can introduce biases and/or artifacts. Recently, genetically modified mouse models have been developed to identify the whole-brain distributions of CRH neurons (Itoi et al., 2014; Kono et al., 2017; Peng et al., 2017; Wamsteeker Cusulin et al., 2013), which has significantly advanced our understanding of the morphological features of CRH neurons in the rodent brain (De Francesco et al., 2015; Garcia et al., 2016; Huang et al., 2013; Nguyen et al., 2016). Advances in whole-brain optical imaging techniques, such as fluorescence micro-optical sectioning tomography (fMOST) (Gong et al., 2016; Gong et al., 2013; Ragan et al., 2012; Zheng et al., 2013), have made it feasible to further quantify cellular distributions and to morphologically reconstruct cells at the whole-brain level. The precision of imaging via fMOST can reveal complex fiber orientations, and can even distinguish individual dendrites. Such quantitative three-dimensional (3D) neuronal morphologies obtained at a brain-wide scale can provide highly accurate arborization details and comprehensive mapping of CRH neuronal connections throughout the brain.

Although the whole-brain expression patterns of CRH have been qualitatively analyzed (Alon et al., 2009; Kono et al., 2017; Peng et al., 2017), high-resolution reconstruction of the full morphologies (including both somata and dendrites) of CRH neurons at the single-neuron level has rarely been performed. Since neuronal morphology is considered to be one of the most defining features to distinguish among neuronal types and network connectivities, characterizing single-neuron morphologies may provide key information on how neuronal information and signals are transmitted within the local networks. Furthermore, analysis of detailed morphological information (including data sets of somatic locations, as well as dendritic and axonal morphological features) of diverse CRH neurons may facilitate in better classifying CRH neuronal types and in revealing their local connectivity. For example, a recent study employed fMOST to investigate CRH distributions in the mouse brain, enabling quantitative analysis of whole-brain CRH somata (Peng et al., 2017) that provides us with substantial quantitative information on brain CRH

networks. However, at present, the morphological details of individual CRH neuronal fibers at the whole-brain level remain poorly understood. In the present study, we constructed a comprehensive whole-brain map of genetically labeled CRH neurons in the mouse brain, which provides dendritic distribution patterns of single CRH neurons. Reconstructions and further analysis showed that heterogeneous CRH interneurons in the mPFC form layer-dependent dendritic-dendritic and dendritic-somatic connections; and that there was a target-oriented distribution of large vesicles (Herring bodies) within the processes of hypothalamic CRH neurons. This work provides a comprehensive description of the whole-brain CRH neuronal distribution pattern and, more importantly, dendritic morphological features of CRH neurons in the mouse brain.

Results

Comparison of morphological features of fluorescent-labeled CRH neurons in three fluorescent-reporter mouse lines

By crossing CRH-IRES-Cre mice with Ai6, Ai14, and Ai32 reporter mice, in which the cassette containing ZsGreen1, td-Tomato, or CHR2-EYFP was expressed in a Cre-dependent manner, we obtained CRH-IRES-Cre;Ai6, CRH-IRES-Cre;Ai14, and CRH-IRES-Cre;Ai32 mice, respectively (Fig. S1A). Then, we compared the distributions and morphologies of fluorescent-labeled CRH neurons in several brain regions, including the olfactory bulb (OB) (Fig. 1A–C), cortex (Fig. 1D–F), PVN (Fig. 1G–I), bed nucleus of the stria terminalis (BST) (Fig. S1B–D) and central nucleus of the amygdala (CeA) (Fig. S1E–G).

In the OB, the transgenic fluorescent proteins were mainly distributed in the glomerular layer (Gl), external plexiform layer (EPl), and the mitral cell layer (Mi) in all three mouse lines. CRH-IRES-Cre;Ai6 mice showed the brightest and largest number of fluorescent-labeled cells in all these layers (Fig. 1A); in particular, more fluorescent cells were labeled in the granule cell layer (GrO) in this mouse line compared to those in CRH-IRES-Cre;Ai14 and CRH-IRES-Cre;Ai32 mice. However, fluorescent-labeled neuronal fibers were short and their fluorescent distributions were not uniform; for example, the dendrites close to the cell bodies of mitral cells were strongly labeled (Fig. 1A, a’, indicated

111 by the arrowheads), but the branches extending to the Gl were not clear (Fig. 1A, a,
112 indicated by the dotted box). CRH-IRES-Cre;Ai14 mice were also labeled with bright cell
113 bodies and dense fibers were labeled in the EPl (Fig. 1B, b'), but only a few dendritic
114 structures were labeled in the Gl (Fig. 1B, b, indicated by the dotted box). By contrast, in
115 each layer of CRH-IRES-Cre;Ai32 mice, the fluorescence distributed in cell bodies and
116 fibers exhibited a uniform brightness (Fig. 1C), and the somata in these sections were
117 organized in a ring-like structure (Fig. 1C, c', indicated by the arrowhead). Unlike the
118 former two mouse lines, the Gl showed a bushy spherical structure (Fig. 1C, c) that was
119 comprised of mitral cells and/or peribulbar cells.

120 In the cortex, fluorescent-labeled cells were found in each layer in CRH-IRES-
121 Cre;Ai6 mice (Fig. 1D). The cell bodies were strongly labeled, while fibers were rarely
122 seen (Fig. 1D, d). The numbers of labeled cells in the cortices of CRH-IRES-Cre;Ai14 and
123 CRH-IRES-Cre;Ai32 mice were less than those in CRH-IRES-Cre;Ai6 mice, and the cells
124 were mainly distributed in layer 2/3 (Fig. 1E–F). Neurons in CRH-IRES-Cre;Ai14 mice
125 also showed clearer and brighter cell bodies (Fig. 1E, e), whereas more fibers were labeled
126 (Fig. 1F) in CRH-IRES-Cre;Ai32 mice, especially in terms of a dense distribution in the
127 first layer (Fig. 1F, f).

128 The outlines of nuclei were clearly visible in the fluorescent labeling of CRH neurons
129 in the PVN (Fig. 1G–I, indicated by the dotted line), BST (Fig. S1B–D, indicated by the
130 dotted box) and CeA (Fig. S1E–G, indicated by the dotted box) of the three mouse lines.
131 Similarly, CRH-IRES-Cre;Ai6 mice showed the highest number of labeled neurons with
132 brighter cell bodies in these three regions (Fig. 1G; Fig. S1B, a and Fig. S1E, d). In CRH-
133 IRES-Cre;Ai14 mice, distinguishable cell bodies and dense fibers were labeled in the BST
134 (Fig. S1C, b) and CeA (Fig. S1F, e), while only the cell bodies were clearly seen in the
135 PVN (Fig. 1H, indicated by the dotted line). By contrast, CRH-IRES-Cre;Ai32 mice
136 showed dense fibers in all of these regions, and the fluorescent signals of the cell bodies
137 were distinguishable (Fig. 1I, Fig. S1D, c and Fig. S1G, f); especially in the PVN, neuronal
138 fibers extending to the lateral and third ventricle (Fig. 1I, i, fibers indicated by the
139 arrowheads) were visible, and there was a uniform fluorescent intensity distributed in the
140 nearby cell bodies and fibers.

141 In summary, among the three reporter mouse lines, CRH-IRES-Cre;Ai6 and CRH-
142 IRES-Cre;Ai14 mice showed clearer and brighter cell bodies of CRH neurons. CRH-IRES-
143 Cre;Ai6 mice had the largest number of labeled CRH cells in each brain region, but almost
144 no neuronal fibers were visible. CRH-IRES-Cre;Ai14 mice showed clear but incomplete
145 fibers. Only CRH-IRES-Cre;Ai32 mice showed the most complete fibrous structures,
146 especially in terms of distributions in neuronal terminals (e.g., the bushy spherical
147 structures in the glomerular layer of the OB; the extended fibers in the cortex and PVN);
148 Regardless of its weaknesses on distinguishing single cell bodies, the fluorescent
149 distributions in were uniform, which is conducive to the adjustment of exposure and the
150 collection of complete morphologies of neurons during imaging.
151
152 **Whole-brain distributions of CRH neurons at high resolution in the CRH-IRES-**
153 **Cre;Ai32 mouse line**
154 Since the single-cell morphology of CRH neurons was most clearly visible in CRH-
155 IRES-Cre;Ai32 mice, we used this mouse line to image EYFP-labeled CRH neurons
156 throughout the brain at a resolution of 0.2 × 0.2 × 1.0 μm via an fMOST system. First, 100-
157 μm down-sampled coronal projection sections (Fig. 2A) were provided to show the overall
158 distributions of CRH neurons in various brain regions. EYFP-labeled cells were distributed
159 in many regions that has not been reported such as in vascular organ of the lamina
160 terminalis (VOLT), ventromedial preoptic nucleus (VMPO), caudate putamen (CPu), bed
161 nucleus of the anterior commissure (BAC), triangular septal nucleus (TS), suprachiasmatic
162 nucleus (SCN), Ko¨lliker-Fuse nucleus (KF) and nucleus X (X) (Fig. 2A). Furthermore,
163 bundles of CRH projection fibers were visible in accumbens nucleus, shell (AcbSh),
164 interstitial nucleus of the posterior limb of the anterior commissure (IPAC), anterior
165 commissure, posterior (acp), corpus callosum (cc), and inferior cerebellar peduncle (icp)
166 (Fig. 2A, indicated by arrowheads and Fig. 2B). The movies of serial sections showed that
167 the fibers in AcbSh, IPAC, and acp were projections from neurons in the OB (Movie S1)
168 and fibers in icp were projections from IO CRH neurons (Movie S2). Moreover, we found
169 novel populations of CRH-positive neurons in some brain regions, such as a sparsely
170 distributed group in the CPu (Fig. 2C) that had dendrites that were radially distributed (with

171 the maximum radius from the terminals to the somata being 40–70 μm). Neurons gathered
172 in the BAC (Fig. 2D) had round cell bodies and two short processes. The average number
173 of CRH-positive neurons found in the SCN was 45.67±0.88, and nearly every neuron had
174 two thick primary dendrites with few branches (Fig. 2E). Neurons in the dorsal cochlear
175 nucleus (DC) (Fig. 2F) had dense apical dendrites distributed in the superficial glial zone,
176 and chandelier cells with apical dendrites vertically distributed were labeled in the
177 cerebellum (Fig. 2G). A cluster of swollen structures (Fig. 2H, indicated by arrowheads)
178 presenting transparent smooth surfaces was visible around the third ventricle (3V) and
179 always extended to the 3V border. Densely labeled vascular-like structures and terminals
180 of CRH neurons were found in VOLT (Fig.2 I) and ME (Fig. 2J). The distributions and
181 morphologies of CRH neurons in other brain regions are shown in Fig. S2.

182 **Three-dimensional distributions and single-cell reconstructions of CRH neurons in**
183 **several brain regions**

184 We reconstructed EYFP-labeled CRH neurons in several brain regions (Fig. 3A–H),
185 including the OB (Fig. 3 A), dorsal part of lateral septal nucleus (LSD) (Fig. 3B), BST (Fig.
186 3C), CeA (Fig. 3D), VMPO (Fig. 3E), hippocampus (Hip) (Fig. 3F), SCN (Fig. 3G), and
187 DC (Fig. 3H). We found that the reconstructed neurons in several brain regions (e.g., mPFC,
188 BST, VMPO, anterior parvicellular part of paraventricular hypothalamic nucleus (PaAp),
189 periventricular hypothalamic nucleus (Pe), and SCN) shared similar morphological
190 characteristics consistent with bipolar neurons (Fig. 3I). CRH neurons in the LSD had the
191 largest average volume of somata (1632±159.6 μm^3) (Fig. 3J) and the longest dendritic
192 length (1.9±0.2 mm) (Fig. 3K). Dendritic length significantly increased as a function of
193 somatic volume (R2=0.597, P=0.0032) (Fig. 3N). CRH neurons in the VMPO also had a
194 larger cell bodies (1172±228.1 μm^3) (Fig. 3J), but the number of dendritic branches
195 (15.2±3.7) (Fig.3 L) and dendritic length (1.1±0.1 mm) (Fig. 3K) were less than those of
196 neurons in the LSD. Dendritic length was also positively correlated with somatic volume
197 in the VMPO (Fig. 3O). Sholl analysis showed that neurons in the LSD had the largest
198 maximum number of intersections, while the VMPO had the least maximum number of
199 intersections. For all of these regions, the maximum numbers of intersections were located

200 at radial distances of 50–100 μm from the somata (Fig. 3M). The more complex dendrites
201 of CRH neurons in the LSD, compared to those in other areas, suggested that CRH neurons
202 in the LSD may receive comparatively more inputs. Most of the dendritic morphologies of
203 CRH neurons in the hippocampus exhibited a similar pattern of an umbrella shape of
204 upward dendrites (Fig. 3F). CRH neurons in the SCN were scattered throughout the nucleus
205 and the dendrites were interlaced with one another (Fig. 3G). We next compared the
206 parameters of all reconstructed neurons (Table S1) in different brain regions and found that
207 CRH neurons in hypothalamic regions—including the PaAp (640.1±60.4 μm^3), Pe
208 (951.2±108.3 μm^3), and SCN (636.0±55.4 μm^3)—had smaller somatic volumes (Fig. 5J
209 and Table S1). Similarly, there were also shorter dendritic lengths of CRH neurons in the
210 PaAp (0.5±0.02 mm), Pe (0.5±0.06 mm), and SCN (0.6±0.05 mm) (Fig. 3K and Table S1).
211 The simpler morphologies of hypothalamic CRH neurons may be related to their endocrine
212 and other conserved functions.
213
214 **Multiple morphological types of CRH neurons form distinct dendritic connections in**
215 **the medial prefrontal cortex (mPFC)**
216 Recent studies have shown that CRH neurons in the mPFC play a critical role in higher
217 cognitive functions (Chen et al., 2020; Hupalo et al., 2019b). In the prelimbic cortex (PrL)
218 within the mPFC, we reconstructed the entire somata (Fig. 4A, purple bodies) and dendrites
219 (Fig. 4A, color lines) of EYFP-labeled CRH neurons within a column that had a volume of
220 350 × 500 × 500 μm. The cell bodies of these neurons were mostly distributed within layers
221 2–4 and most of their dendrites were vertically distributed. There were dendritic branches
222 in both the upper and lower parts of the somata. The apical dendrites that branched in the
223 first layer formed a dense dendritic network, and most of them reached the pia mater (Fig.
224 4A, reconstructed fibers indicated in layer 1); furthermore, the basal dendrites extended
225 and branched into layer 4 at a distance of approximately 500 μm from the cortical surface
226 (Fig. 4A, reconstructed fibers indicated in layer 4). Individual reconstructed neurons were
227 classified according to the distances (50–100, 100–150, 150–200, 200–250, and >250 μm)
228 between their somata and the surface of the cortex (Fig. 4B), and the percentages of neurons
229 in these categories were 19%, 31%, 35%, 10%, and 5%, respectively (Fig. 4B, indicated in

230 the pie chart). We found that there was significant correlation between the somatic depth
231 (distance from the cortical surface) and both the total dendritic length (Fig. 4C, upper half,
232 r=0.4440) and total Euclidean distance (the straight-line distance from the soma to the
233 given point of the dendrite) (Fig. 4C, bottom half, r=0.5399). Sholl analyses showed that
234 the number of intersections with a radial distance from the soma being less than 50 μm was
235 larger in neurons with a somatic depth of 50–100 μm than that of neurons with a somatic
236 depth of 100–150 μm; in contrast, the number of intersections with a radial distance from
237 the soma being more than 50 μm was smaller and ended at approximately 100 μm of the
238 radial distance from the soma in neurons with a somatic depth of 50–100 μm. Interesting,
239 the maximum numbers of intersections were similar between these two types of neurons
240 (Fig. 4D). We also found that the total dendritic length (Fig. 4E, left half) and the total
241 Euclidean distance (Fig. 4E, right half) of neurons with a somatic depth of less than 100
242 μm were significantly smaller than those with somatic depths of 100–150 μm (P=0.0285)
243 and more than 150 μm (P=0.0005), while there were no significant differences in the total
244 number of dendritic branches or the total number of dendritic terminal points (Fig. S3I).
245 The average dendritic lengths of neurons at somatic depths of less than 100 μm, 100–150
246 μm, and more than 100–150 μm were 0.82±0.26, 1.33±0.54, and 1.48±0.68 mm,
247 respectively; furthermore, their total Euclidean distances were 14.65±5.19, 38.77±25.49,
248 and 48.67±30.38 mm, and their total numbers of dendritic branches were 23.23±8.65,
249 32.86±20.28, 33.32±19.44, respectively.

250 To investigate local CRH-CRH connection patterns within the cortex, we divided
251 CRH-CRH connections into three types (Fig. 4F–H). Type I consisted of basal-to-apical
252 connections. Here, somata in layer 2 sent dendrites downward (the green cell of fig.4 F-a)
253 that contacted with the upward dendrites (the purple cell of Fig. 4F, a) from the somata in
254 layer 3 (as shown in the red dotted box of Fig. 4F, a and b). Type II consisted of basal-to-
255 somatic connections (as shown in the yellow dotted box of Fig. 4G, c and d). In layer 2–3,
256 a soma in the upper layer sent dendrites downward (as shown in Fig. 4G, c, red cell), and
257 the end of one branch (Fig.4 G-d red arrows) was in contact with an adjacent lower cell
258 body (Fig. 4G, c, orange cell; Fig. 4G, d, orange arrows). Type III consisted of basal-to-
259 basal connections (Fig. 4G, c and e; Fig. 4H, f, green dotted box). Two cell bodies in layer

260 2–3 sent dendrites downward, and the end of one branch (Fig. 4G, e, red arrows; Fig. 4H,
261 g, yellow arrows) from the upper soma and the branch (Fig. 4G, e, orange arrows; Fig. 4H,
262 g, blue arrows) from the lower soma formed a connection. A common feature of the three
263 types of connections was that the fluorescent intensity increased at the contact point,
264 indicating a possible connection of structures (Fig. 4F, b, G, d and e, and H, g, purple
265 arrows). The connections of type II and type III are demonstrated in movie S3.
266 We next performed immunofluorescent staining to determine the specificity of EYFP-
267 labeled neurons in CRH-IRES-Cre;Ai32 mice. The results showed that most of the EYFP-
268 labeled neurons in the mPFC were co-labeled with CRH antibodies (Fig. S3 A–C, indicated
269 by white arrow). Interestingly, in adult hybrid mice, EYFP-labeled pyramidal neurons were
270 visible in layer 3 or layer 5 of the cortex (Fig. S3F), but there were no EYFP-labeled
271 pyramidal neurons on the 21st day after birth (Fig. S3E). These pyramidal neurons did not
272 co-exist with CRH antibodies (Fig. S3G), including their dendrites and spines (Fig. S3, a,
273 indicated by arrowheads). We also observed that some EYFP-labeled neurite swellings in
274 layer 1 were also labelled with CRH antibodies (Fig. S3 b, indicated by arrowheads).
275
276 **Reconstructions and morphological features of CRH neurons in the PaAp and Pe**
277 Hypothalamic neuroendocrine CRH neurons play an important role in stress responses,
278 but neurons within different subregions require more detailed morphological analysis. We
279 chose EYFP-labeled neurons in the PaAP and Pe to reconstruct their somata and processes
280 (Fig. 5A and C; Fig. S4D and E). There was a noteworthy co-localization pattern (Fig.
281 S4A–C) for the EYFP-labeled signals and CRH antibodies in the PaAP. There were
282 vesicular fluorescent labels (Herring bodies) (Fig. 5B and D, grey reconstructed structures)
283 on the neurites of neurons in both the PaAP and Pe, and they also co-labeled with CRH
284 antibodies (Fig. 5E, indicated by arrowheads). In terms of their 3D patterns, the somata of
285 some neurons (Fig. 5A–B, purple reconstructed cell bodies) distributed in the PaAP sent
286 out fibers rostrally (Fig. 5A–B, red lines), and there were spaced and small Herring bodies
287 (Fig. 5B, b–d, grey bodies) on these fibers. An example of these reconstructed cells is
288 shown (Fig. 5B) according to the primary branches and number of Herring bodies, and
289 there were four distribution patterns of these neurons. Pattern 1 (Fig. 5B, a) consisted of

290 cells that had two primary branches with the shortest fiber length and no Herring bodies.
291 Pattern 2 (Fig. 5B, b) consisted of cells that had two primary branches with similar fiber
292 lengths at both ends of the somata and were distributed almost vertically, and the fibers
293 extending rostrally had Herring bodies. Pattern 3 (Fig. 5B, c) consisted of cells with both
294 ends of the fibers having Herring bodies and the one fiber branch that was distributed
295 horizontally was longer and extended rostrally, whereas the other short branch was
296 distributed vertically. Finally, pattern 4 (Fig. 5B, d) consisted of fibers of multipolar cells
297 extending rostrally having Herring bodies and being distributed horizontally. The locations
298 of the reconstructed somata in the PaAP are shown in Fig. S4D (purple bodies indicated by
299 red circles).

300 In the Pe, the reconstructed somata were located in the lower part of the PaAp and
301 around the 3V (Fig. 5 C, purple bodies; Fig. S4E indicated by red circles). These cells sent
302 out fibers and one or two of them extended close to the 3V (Fig. 5C and D, red line). There
303 were large Herring bodies on the fibers (Fig. 5D, grey reconstituted bodies; Fig. 5F,
304 indicated by yellow arrowheads) and they terminated in the ependymal cell layer adjacent
305 to the 3V (Fig. 5F). Most of the reconstructed cells within the Pe were bipolar neurons (Fig.
306 5D, e and f), and the fibers extending downward to the 3V had more Herring bodies (Fig.
307 5D, f and g).

308 Next, we compared the somatic and fiber parameters of the neurons in the PaAP and
309 Pe and found that the average volume of the soma in the Pe (951.2±108.3 μm^3) was larger
310 than that in the PaAP (640.1±60.4 μm^3) (Fig. 5G, P=0.0119), and the number of Herring
311 bodies in the Pe (19.4±2.5) was significantly greater than that in the PaAP (7.9±1.6) (Fig.
312 5H, P=0.0005). The total Herring-body volume (2678±652.3 μm^3) (Fig. 5I, P=0.0003) per
313 cell and the average volume of Herring bodies (153.4±43.1 μm^3) (Fig. 5J, P=0.0047) in the
314 Pe were significantly larger than those (468.2±79.2 μm^3 and 47.7±5.3 μm^3) in the PaAP.
315 We also found that there was a negative correlation between the number of Herring bodies
316 and the soma volume in the PaAP (r=−0.4519, P=0.0455) (Fig. 5K). There was no
317 significant difference in the total fibrous length (PaAP: 455.4±24.1 μm, Pe: 537.5±57.6 μm)
318 (Fig. 5L) or the total number of fibrous branches (PaAP: 5.4±0.9, Pe: 6.3±1.6) (Fig. 5M)
319 of neurons in the PaAP and Pe. We found that most (75% in the PaAP and 70% in the Pe)

(Fig. 5N, right half, indicated in the pie chart) of the reconstructed neurons were bipolar neurons, which were characterized by the number of primary fibrous branches (Fig. 5N, left half).

Collectively, these 3D reconstructions of hypothalamic CRH neurons may be indicative of the transport and storage of CRH peptides in hypothalamic neurons, as well as the possible their release sites, such as the third ventricle. These findings provide a structural basis for further elucidating the neural circuits and functions of CRH neurons.

Discussion

During the last few decades, transgenic rodent models have become powerful tools for studying the distribution (Chen et al., 2015; Kono et al., 2017; Wamsteeker Cusulin et al., 2013) and function (Kolber et al., 2010; Lu et al., 2008; Regev et al., 2012; Stenzel-Poore et al., 1994) of CRH neurons in the brain. In order to probe the morphological characteristics of CRH neurons at single-cell resolution, we combined genetic labeling (using transgenic mouse lines) with the fMOST platform to generate high-resolution imaging datasets, with which we characterized the morphologies of distinct CRH neurons distributed in various brain regions throughout the whole mouse brain.

The robust native fluorescence of each of these reporter mouse lines enabled direct visualization of fine dendritic and axonal structures of labeled neurons, which is demonstrated to be useful for mapping neuronal circuitry, as well as imaging and tracking specific cell populations (Madisen et al., 2010; Taniguchi et al., 2011; Walker et al., 2019). We compared the distribution patterns of fluorescent-labeled CRH neurons in three reporter mouse lines. Notably, the fluorescent fusion protein, CHR2-EYFP, is membrane-bound and is therefore distributed along the plasma membrane of neuronal processes within CRH-IRES-Cre;Ai32 mice (Dedic et al., 2018; Park et al., 2018), which enables a clear visualization of the entire neuronal morphology. Therefore, we utilized CRH-IRES-Cre;Ai32 mice for whole-brain imaging and reconstructions. Interestingly, a large number of EYFP-labeled cortical pyramidal neurons was also observed in adult mice (which has not been reported previously from the onset age of postnatal day 21) (Fig. S3).

Next, we focused our analyses of reconstructed neurons on several stress-related

350 regions, including the mPFC, hypothalamus, amygdala, BST, and hippocampus. For
351 example, it has been reported that local CRH-synthesizing neurons are prominent in the
352 PFC (Charlton et al., 1987; De Souza et al., 1985; Lewis et al., 1989; Merchenthaler et al.,
353 1984; Swanson et al., 1983) and may modulate the activities of pyramidal neurons
354 (Gallopin et al., 2006). However, until now, the complete morphologies of CRH neurons
355 in the mPFC have rarely been reported. Here, we reconstructed fluorescent-labeled CRH
356 neurons in the cortical column in the PrL within mPFC across layers 1–4 (Fig. 4A).
357 Importantly, we classified different neuronal types by their soma depths and arborization
358 patterns (example listed in Fig. 4B). For the first time, we showed the distribution of CRH
359 neurons with different morphological types in different cortical layers. We found there were
360 dense dendrites (Fig. 4A) with dendritic swellings (Fig. S3, b) in layer 1 (the soma of which
361 were located in layer 2/3 or layer 4), and that fibers extended to the surface of the cortex.
362 According to the layer-specific dendritic locations and their different projection targets,
363 several types of putative connection patterns between CRH neurons were identified in the
364 cortex (listed in Fig. 4F–H). Such a diverse dendritic connection pattern of cortical CRH
365 neurons may reflect differential innervation of downstream output targets (each amplified
366 subfigure shown in Fig. 4F–H). Therefore, by characterizing their somatic locations and
367 unique respective local dendritic morphologies of CRH neurons, our present study not only
368 increases our current understanding of the distribution of CRH neurons, but also enables
369 future studies to further elaborate upon cell-specific classifications. Taken together, these
370 findings may help elaborate future functional studies of morphologically diverse CRH
371 neurons in the PFC.

372 Importantly, CRH functions as a neuropeptide hormone produced in neuroendocrine
373 neurons in the PVN and regulates the synthesis and secretion of glucocorticoids from the
374 adrenal glands through the action of adrenocorticotropic hormone. For the first time, we
375 reconstructed the intact morphologies of CRH neurons and their neurite varicosities
376 (Herring bodies) located within fibers in the PaAp (Fig.5 A–B) and Pe CRH neurons (Fig.
377 5C–D). In the PaAp, most fibers with Herring bodies projected rostrally (Fig. 5B), while
378 in the Pe, the ends of the fibers extended to the third ventricle (Fig. 5C–D and F). Since
379 Herring bodies mainly function to store and secrete CRH (Dellmann and Rodriguez, 1970;

380 Vazquez and Amat, 1978; Yamazaki et al., 1981), we speculate that these endocrine CRH
381 neurons are different from those that project to the median eminence, and that CRH may
382 be also secreted to other areas of the hypothalamus or cerebrospinal fluid to participate in
383 its regulatory functions. We further found a negative correlation between somatic volume
384 and Herring body number in the PaAp (Fig. 5K). Thus, our reconstructed morphological
385 characteristics of Herring bodies (located in the fibers of CRH neurons) may facilitate
386 future classifications (according to different fiber orientations and Herring-body
387 distribution patterns) of hypothalamic CRH neurons and advance our understanding of
388 their potentially diverse functions.

389 The reconstructed CRH neurons in different brain regions showed diverse distribution
390 patterns and morphologies (Fig. 3A–H). We found that some neurons shared a common
391 bipolar shape across various brain regions (Fig. 3I), especially in the hypothalamus (75%
392 in the PaAp, 100% in SCN) and cortex. Rho *et al*. reported that parvocellular CRH
393 neuroendocrine neurons typically have two relatively thick primary dendrites that extend
394 from opposite sides of the soma in a bipolar arrangement and branch once (Rho and
395 Swanson, 1989); and furthermore, bipolar cells are commonly found in the cortex (Cahusac
396 et al., 1998; Delville et al., 1992; Yan et al., 1998). Thus, our present study in CRH-reporter
397 mice is consistent with these previous studies and is the first to describe the specific neural
398 structures of these CRH neurons, such as the different types of connections between CRH
399 neurons in the mPFC, as well as the intact morphologies of Herring bodies in hypothalamic
400 CRH neurons. Such simplified branching properties for these CRH neurons in the
401 hypothalamus may be conducive to their endocrine functions. Among all the reconstructed
402 CRH neurons across different brain regions, their somata had different sizes (Fig. 3J), with
403 somata in the LSD, VMPO, and hippocampus being larger than those in the PaAp, Pe, and
404 SCN. Also, we found differential dendritic branch complexities across these regions. For
405 example, CRH neurons in the mPFC, LSD, and hippocampus all exhibited more complex
406 dendritic morphologies compared to those in the PaAP, Pe, and SCN (Fig. 3K–L). Hupalo
407 *et al*. demonstrated that chemogenetic activation of caudal but not rostral dmPFC CRH
408 neurons potently impaired working memory, whereas inhibition of these neurons improved
409 working memory (Hupalo et al., 2019b). In addition, CRH acts in the medial septum to

impair spatial memory (Hupalo et al., 2019a), and acts in the BNST to participate in stress-induced maladaptive behaviors (Hu et al., 2020). However, the functions of CRH in the OB, SCN, and VMPO remain unclear. Therefore, our current study may provide a detailed morphological basis for future functional-based studies for CRH neurons in these different brain regions. Interestingly, the PaAP, Pe, and SCN all belong to the hypothalamus, and CRH neurons in these regions had smaller somata and exhibited more prevalent bipolar branching patterns compared to other brain regions. In the PVN, CRH neurons have been identified as parvocellular cells (Miklos and Kovacs, 2002; Rho and Swanson, 1989). We found that the mean somatic volume of CRH neurons in the Pe was larger than those in the PaAP (Fig. 5G). Hence, we speculate that these data may be indicative of two different types of CRH endocrine neurons within the hypothalamus. Collectively, our quantitative analysis of these reconstructions demonstrates a region-specific diversity of CRH neurons in terms of both somatic size and branching complexity.

In summary, in the present study, we generated high-resolution imaging datasets to characterize, at single-cell resolution, the fine morphologies of CRH neurons distributed in diverse brain regions. Such region-specific reconstructions of intact morphologies of CRH neurons may help in further elucidating both CRH-mediated physiological functions in various brain circuits and the associations of their dysfunction with various neuropathological diseases.

Materials and Methods

Animals

CRH-IRES-Cre (B6(Cg)-Crh$^{tm1(cre)Zjh}$/J; stock number: 012704), Ai6 (B6.Cg-Gt(ROSA)26Sor$^{tm6(CAG-ZsGreen1)Hze}$/J; stock number: 007906), Ai14 (B6.Cg-Gt(ROSA)26Sor$^{tm14(CAG-TdTomato)Hze}$/J; stock number: 007914) and Ai32 (B6;Cg-Gt(ROSA)26Sor$^{tm32(CAG-COP4*H134R/EYFP)Hze}$/J; stock number: 012569) mice have been described previously(Madisen et al., 2012; Madisen et al., 2010; Taniguchi et al., 2011). CRH-IRES-Cre, Ai6 and Ai32 mice were purchased from the Jackson Laboratory. Ai14 mice were obtained from the laboratory of Minmin Luo (NIBS, China). All of the mice were bred onto a C57BL/6J genetic background. CRH-IRES-Cre;Ai6, CRH-IRES-

440 Cre;Ai14 and CRH-IRES-Cre;Ai32 mice were derived from crosses of the CRH-IRES-Cre
441 and Ai6,Ai14 and Ai32 genotypes, respectively. Male mice at 12 weeks of age were used
442 for experiment. CRH-IRES-Cre;Ai32 male mice were used for fMOST imaging and
443 neuron reconstructions. The mice were housed on a 12-hour light/dark cycle with food and
444 water ad libitum. All the animal experiments were performed according to the procedures
445 approved by the Institutional Animal Ethics Committee of University of Science and
446 Technology of China.
447
448 **Histology**
449 All histological procedures have been previously described(Gong et al., 2016; Xiong
450 et al., 2014; Yang et al., 2013). Briefly, for whole-brain imaging, the mice were
451 anaesthetized and perfused with 0.01M PBS (Sigma-Aldrich Inc., St. Louis, USA),
452 followed by 4% paraformaldehyde (PFA) and 2.5% sucrose in 0.01M PBS. The brains were
453 excised and post-fixed in 4% PFA for 24 h. After fixation, each intact brain was rinsed
454 overnight at 4°C in 0.01M PBS and subsequently dehydrated in a graded ethanol series.
455 Then, the brains were impregnated with Glycol Methacrylate (GMA, Ted Pella Inc.,
456 Redding, CA) and embedded in a vacuum oven.
457 For immunofluorescence and visualizing fluorescent labeled neurons in three kinds of
458 mice lines, the fixed brains were embedded by agarose and consecutive 50 or 100 μm
459 coronal sections were collected using a vibration microtome (Leica VT1200S, Germany).
460 For CRH immunofluorescence, 50 μm sections were washed in PBS three times (10 min
461 each time) and permeabilized with 0.3% Triton X-100 for 30 min, followed by 5% normal
462 donkey serum blocking solution at room temperature for 1 h. Sections were then incubated
463 with rabbit anti-CRF (1:2,000, Bachem, T4037) primary antibody in PBS containing 0.3%
464 Triton X-100 overnight or for 36 h at 4°C. After washing in PBS, sections were incubated
465 with Alexa Fluor 594-conjugated donkey anti-rabbit secondary antibody (1:200, Jackson
466 Immuno Research, 711-585-152) diluted in 0.1% Triton X-100 in PBS at room temperature
467 for 2 h. After washing in PBS, sections were mounted on slides with antifade mounting
468 medium (Vector Laboratories, Inc, H-1000) and stored at 4°C. For visualizing fluorescent

469 labeled neurons, 100 μm sections were washed in PBS and mounted on slides. All images
470 were photographed using LSM 880 (Zeiss, Germany) confocal microscope.
471
472 **Whole-brain imaging**
473 Whole-brain imaging was performed by the fMOST system(Gong et al., 2016). Briefly,
474 the immersed samples were fixed on the imaging plane, a WVT system automatically
475 performed the sectioning and imaging to complete the brain-wide data acquisition. We
476 acquired the data sets after sectioning at a 1 um thickness and imaging at a 0.32 x 0.32 x1
477 um voxel size. To enhance the in-focus EYFP signal, we added Na_2CO_3 into the water bath.
478 Most of the EYFP molecules were preserved in a nonfluorescent state, rather than directly
479 damaged, through chromophore protonation during the resin-embedding procedure. These
480 fluorescent signals were chemically recovered to the fluorescent state using 0.05 M Na_2CO_3
481 during imaging. For the CRH-IRIS-Cre;Ai32 samples, real-time PI staining was performed.
482
483 **Image preprocessing**
484 The raw data acquired by the fMOST system needed image preprocessing for mosaic
485 stitching and illumination correction. This process has been described before(Gong et al.,
486 2016). Briefly, the mosaics of each coronal section were stitched to obtain an entire section
487 based on accurate spatial orientation and adjacent overlap. Lateral illumination correction
488 was performed section by section. Image preprocessing was implemented in C++ and
489 optimized in parallel using the Intel MPI Library (v.3.2.2.006, Intel). The whole data sets
490 were executed on a computing server (72 cores, 2GHz per core) within 6h. All full coronal
491 sections were saved at an 8-bit depth in LZW compression TIFF format after image
492 preprocessing.
493
494 **Visualization and reconstruction.**
495 We visualized the data set using Amira software (v.5.2.2, FEI) and Imaris software
496 (v.9.2.1, bitplane, Switzerland) to generate the figures and movies. To process the TB-sized
497 data on a single workstation, we transformed the data format from TIFF to the native LDA
498 type using Amira. The visualization process included extracting the data in range of interest,

sampling or interpolation, reslicing the images, identifying the maximum intensity projection, volume and surface rendering, and generating the Movies using the main module of Amira. The segmentation editor module of Amira was utilized for the manual outline segmentation of the third ventricle, somata and Herring bodies. We applied the filament editor module of Amira to trace the morphology of EYFP-labeled neurons in 3D by human-machine interaction. The reconstructed neurons were checked back-to-back by three persons. The tracing results with original position information were saved in SWC format and the results of the analyses were generated by L-Measure software (v.5.3).

Statistics

All statistical graphs were generated using Graphpad Prism v.6.01. Two-tailed Student's t-test and one-way ANOVA followed by Tukey's post hoc tests were also performed using Graphpad Prism v.6.01 and SPSS (IBM SPSS Statistics 23).The confidence level was set to 0.05 (P value) and all results were presented as the means ± S.E.M.

Acknowledgments

We thank Dr. Minmin Luo (NIBS) for providing the Ai14 mice; Xingning Li, Miao Ren, Beng Long, Jie Peng, Yuxin Li (HUST), Hui Fang, Xinya Qin, and Penghao Luo (USTC) for help with the experiment.

Competing interests

The authors have no conflicts of interest to declare.

References

Albeck, D.S., McKittrick, C.R., Blanchard, D.C., Blanchard, R.J., Nikulina, J., McEwen, B.S., and Sakai, R.R. (1997). Chronic social stress alters levels of corticotropin-releasing factor and arginine vasopressin mRNA in rat brain. J Neurosci *17*, 4895-4903.

Alon, T., Zhou, L., Perez, C.A., Garfield, A.S., Friedman, J.M., and Heisler, L.K. (2009). Transgenic mice expressing green fluorescent protein under the control of the corticotropin-releasing hormone promoter. Endocrinology *150*, 5626-5632.

Bassett, J.L., and Foote, S.L. (1992). Distribution of corticotropin-releasing factor-like immunoreactivity in squirrel monkey (Saimiri sciureus) amygdala. J Comp Neurol *323*, 91-102.

532 Cahusac, P.M., Castro, M.G., Robertson, L., and Lowenstein, P.R. (1998). Electrophysiological
533 evidence against a neurotransmitter role of corticotropin-releasing hormone (CRH) in primary
534 somatosensory cortex. Brain Res *793*, 73-78.
535 Charlton, B.G., Ferrier, I.N., and Perry, R.H. (1987). Distribution of corticotropin-releasing factor-
536 like immunoreactivity in human brain. Neuropeptides *10*, 329-334.
537 Chen, P., Lou, S., Huang, Z.H., Wang, Z., Shan, Q.H., Wang, Y., Yang, Y., Li, X., Gong, H., Jin, Y.*, et al.*
538 (2020). Prefrontal Cortex Corticotropin-Releasing Factor Neurons Control Behavioral Style
539 Selection under Challenging Situations. Neuron *106*, 301-315 e307.
540 Chen, Y., Molet, J., Gunn, B.G., Ressler, K., and Baram, T.Z. (2015). Diversity of Reporter Expression
541 Patterns in Transgenic Mouse Lines Targeting Corticotropin-Releasing Hormone-Expressing
542 Neurons. Endocrinology *156*, 4769-4780.
543 Cummings, S.L. (1989). Distribution of corticotropin-releasing factor in the cerebellum and
544 precerebellar nuclei of the cat. J Comp Neurol *289*, 657-675.
545 De Francesco, P.N., Valdivia, S., Cabral, A., Reynaldo, M., Raingo, J., Sakata, I., Osborne-Lawrence,
546 S., Zigman, J.M., and Perello, M. (2015). Neuroanatomical and functional characterization of CRF
547 neurons of the amygdala using a novel transgenic mouse model. Neuroscience *289*, 153-165.
548 De Souza, E.B., Insel, T.R., Perrin, M.H., Rivier, J., Vale, W.W., and Kuhar, M.J. (1985). Corticotropin-
549 releasing factor receptors are widely distributed within the rat central nervous system: an
550 autoradiographic study. J Neurosci *5*, 3189-3203.
551 Dedic, N., Kuhne, C., Jakovcevski, M., Hartmann, J., Genewsky, A.J., Gomes, K.S., Anderzhanova,
552 E., Pohlmann, M.L., Chang, S., Kolarz, A.*, et al.* (2018). Chronic CRH depletion from GABAergic,
553 long-range projection neurons in the extended amygdala reduces dopamine release and increases
554 anxiety. Nat Neurosci *21*, 803-807.
555 Dellmann, H.D., and Rodriguez, E.M. (1970). Herring bodies; an electron microscopic study of local
556 degeneration and regeneration of neurosecretory axons. Z Zellforsch Mikrosk Anat *111*, 293-315.
557 Delville, Y., Stires, C., and Ferris, C.F. (1992). Distribution of corticotropin-releasing hormone
558 immunoreactivity in golden hamster brain. Brain Res Bull *29*, 681-684.
559 Foote, S.L., and Cha, C.I. (1988). Distribution of corticotropin-releasing-factor-like
560 immunoreactivity in brainstem of two monkey species (Saimiri sciureus and Macaca fascicularis):
561 an immunohistochemical study. J Comp Neurol *276*, 239-264.
562 Gallopin, T., Geoffroy, H., Rossier, J., and Lambolez, B. (2006). Cortical sources of CRF, NKB, and
563 CCK and their effects on pyramidal cells in the neocortex. Cereb Cortex *16*, 1440-1452.
564 Garcia, I., Bhullar, P.K., Tepe, B., Ortiz-Guzman, J., Huang, L., Herman, A.M., Chaboub, L., Deneen,
565 B., Justice, N.J., and Arenkiel, B.R. (2016). Local corticotropin releasing hormone (CRH) signals to
566 its receptor CRHR1 during postnatal development of the mouse olfactory bulb. Brain Struct Funct
567 *221*, 1-20.
568 Gong, H., Xu, D., Yuan, J., Li, X., Guo, C., Peng, J., Li, Y., Schwarz, L.A., Li, A., Hu, B.*, et al.* (2016).
569 High-throughput dual-colour precision imaging for brain-wide connectome with cytoarchitectonic
570 landmarks at the cellular level. Nat Commun *7*, 12142.
571 Gong, H., Zeng, S., Yan, C., Lv, X., Yang, Z., Xu, T., Feng, Z., Ding, W., Qi, X., Li, A.*, et al.* (2013).
572 Continuously tracing brain-wide long-distance axonal projections in mice at a one-micron voxel
573 resolution. Neuroimage *74*, 87-98.
574 Hu, P., Liu, J., Maita, I., Kwok, C., Gu, E., Gergues, M.M., Kelada, F., Phan, M., Zhou, J.N., Swaab,
575 D.F.*, et al.* (2020). Chronic Stress Induces Maladaptive Behaviors by Activating Corticotropin-
576 Releasing Hormone Signaling in the Mouse Oval Bed Nucleus of the Stria Terminalis. J Neurosci.
577 Huang, L., Garcia, I., Jen, H.I., and Arenkiel, B.R. (2013). Reciprocal connectivity between mitral

578 cells and external plexiform layer interneurons in the mouse olfactory bulb. Front Neural Circuits
579 *7*, 32.
580 Hupalo, S., Bryce, C.A., Bangasser, D.A., Berridge, C.W., Valentino, R.J., and Floresco, S.B. (2019a).
581 Corticotropin-Releasing Factor (CRF) circuit modulation of cognition and motivation. Neurosci
582 Biobehav Rev *103*, 50-59.
583 Hupalo, S., Martin, A.J., Green, R.K., Devilbiss, D.M., and Berridge, C.W. (2019b). Prefrontal
584 Corticotropin-Releasing Factor (CRF) Neurons Act Locally to Modulate Frontostriatal Cognition and
585 Circuit Function. J Neurosci *39*, 2080-2090.
586 Itoi, K., Talukder, A.H., Fuse, T., Kaneko, T., Ozawa, R., Sato, T., Sugaya, T., Uchida, K., Yamazaki, M.,
587 Abe, M.*, et al.* (2014). Visualization of corticotropin-releasing factor neurons by fluorescent
588 proteins in the mouse brain and characterization of labeled neurons in the paraventricular nucleus
589 of the hypothalamus. Endocrinology *155*, 4054-4060.
590 Kolber, B.J., Boyle, M.P., Wieczorek, L., Kelley, C.L., Onwuzurike, C.C., Nettles, S.A., Vogt, S.K., and
591 Muglia, L.J. (2010). Transient early-life forebrain corticotropin-releasing hormone elevation causes
592 long-lasting anxiogenic and despair-like changes in mice. J Neurosci *30*, 2571-2581.
593 Kono, J., Konno, K., Talukder, A.H., Fuse, T., Abe, M., Uchida, K., Horio, S., Sakimura, K., Watanabe,
594 M., and Itoi, K. (2017). Distribution of corticotropin-releasing factor neurons in the mouse brain:
595 a study using corticotropin-releasing factor-modified yellow fluorescent protein knock-in mouse.
596 Brain Struct Funct *222*, 1705-1732.
597 Lewis, D.A., Foote, S.L., and Cha, C.I. (1989). Corticotropin-releasing factor immunoreactivity in
598 monkey neocortex: an immunohistochemical analysis. J Comp Neurol *290*, 599-613.
599 Lu, A., Steiner, M.A., Whittle, N., Vogl, A.M., Walser, S.M., Ableitner, M., Refojo, D., Ekker, M.,
600 Rubenstein, J.L., Stalla, G.K.*, et al.* (2008). Conditional mouse mutants highlight mechanisms of
601 corticotropin-releasing hormone effects on stress-coping behavior. Mol Psychiatry *13*, 1028-1042.
602 Madisen, L., Mao, T., Koch, H., Zhuo, J.M., Berenyi, A., Fujisawa, S., Hsu, Y.W., Garcia, A.J., 3rd, Gu,
603 X., Zanella, S.*, et al.* (2012). A toolbox of Cre-dependent optogenetic transgenic mice for light-
604 induced activation and silencing. Nat Neurosci *15*, 793-802.
605 Madisen, L., Zwingman, T.A., Sunkin, S.M., Oh, S.W., Zariwala, H.A., Gu, H., Ng, L.L., Palmiter, R.D.,
606 Hawrylycz, M.J., Jones, A.R.*, et al.* (2010). A robust and high-throughput Cre reporting and
607 characterization system for the whole mouse brain. Nat Neurosci *13*, 133-140.
608 Merchenthaler, I. (1984). Corticotropin releasing factor (CRF)-like immunoreactivity in the rat
609 central nervous system. Extrahypothalamic distribution. Peptides *5 Suppl 1*, 53-69.
610 Merchenthaler, I., Hynes, M.A., Vigh, S., Schally, A.V., and Petrusz, P. (1984). Corticotropin releasing
611 factor (CRF): origin and course of afferent pathways to the median eminence (ME) of the rat
612 hypothalamus. Neuroendocrinology *39*, 296-306.
613 Mezey, E., Kiss, J.Z., Skirboll, L.R., Goldstein, M., and Axelrod, J. (1984). Increase of corticotropin-
614 releasing factor staining in rat paraventricular nucleus neurones by depletion of hypothalamic
615 adrenaline. Nature *310*, 140-141.
616 Miklos, I.H., and Kovacs, K.J. (2002). GABAergic innervation of corticotropin-releasing hormone
617 (CRH)-secreting parvocellular neurons and its plasticity as demonstrated by quantitative
618 immunoelectron microscopy. Neuroscience *113*, 581-592.
619 Miyata, M., Okada, D., Hashimoto, K., Kano, M., and Ito, M. (1999). Corticotropin-releasing factor
620 plays a permissive role in cerebellar long-term depression. Neuron *22*, 763-775.
621 Nguyen, A.Q., Dela Cruz, J.A., Sun, Y., Holmes, T.C., and Xu, X. (2016). Genetic cell targeting
622 uncovers specific neuronal types and distinct subregions in the bed nucleus of the stria terminalis.
623 J Comp Neurol *524*, 2379-2399.

624 Park, S.J.H., Pottackal, J., Ke, J.B., Jun, N.Y., Rahmani, P., Kim, I.J., Singer, J.H., and Demb, J.B. (2018).
625 Convergence and Divergence of CRH Amacrine Cells in Mouse Retinal Circuitry. J Neurosci *38*,
626 3753-3766.
627 Peng, J., Long, B., Yuan, J., Peng, X., Ni, H., Li, X., Gong, H., Luo, Q., and Li, A. (2017). A Quantitative
628 Analysis of the Distribution of CRH Neurons in Whole Mouse Brain. Front Neuroanat *11*, 63.
629 Puder, B.A., and Papka, R.E. (2001). Distribution and origin of corticotropin-releasing factor-
630 immunoreactive axons in the female rat lumbosacral spinal cord. J Neurosci Res *66*, 1217-1225.
631 Ragan, T., Kadiri, L.R., Venkataraju, K.U., Bahlmann, K., Sutin, J., Taranda, J., Arganda-Carreras, I.,
632 Kim, Y., Seung, H.S., and Osten, P. (2012). Serial two-photon tomography for automated ex vivo
633 mouse brain imaging. Nat Methods *9*, 255-258.
634 Regev, L., Tsoory, M., Gil, S., and Chen, A. (2012). Site-specific genetic manipulation of amygdala
635 corticotropin-releasing factor reveals its imperative role in mediating behavioral response to
636 challenge. Biol Psychiatry *71*, 317-326.
637 Rho, J.H., and Swanson, L.W. (1989). A morphometric analysis of functionally defined
638 subpopulations of neurons in the paraventricular nucleus of the rat with observations on the
639 effects of colchicine. J Neurosci *9*, 1375-1388.
640 Sasaki, M., and Sato, H. (2013). Polysynaptic connections between Barrington's nucleus and sacral
641 preganglionic neurons. Neurosci Res *75*, 150-156.
642 Shu, Y.M., Ni, R.J., Sun, Y.J., Fang, H., and Zhou, J.N. (2015). Distribution of corticotropin-releasing
643 factor in the tree shrew brain. Brain Res *1618*, 270-285.
644 Spiess, J., Villarreal, J., and Vale, W. (1981). Isolation and sequence analysis of a somatostatin-like
645 polypeptide from ovine hypothalamus. Biochemistry *20*, 1982-1988.
646 Stenzel-Poore, M.P., Heinrichs, S.C., Rivest, S., Koob, G.F., and Vale, W.W. (1994). Overproduction
647 of corticotropin-releasing factor in transgenic mice: a genetic model of anxiogenic behavior. J
648 Neurosci *14*, 2579-2584.
649 Swanson, L.W., Sawchenko, P.E., Rivier, J., and Vale, W.W. (1983). Organization of ovine
650 corticotropin-releasing factor immunoreactive cells and fibers in the rat brain: an
651 immunohistochemical study. Neuroendocrinology *36*, 165-186.
652 Taniguchi, H., He, M., Wu, P., Kim, S., Paik, R., Sugino, K., Kvitsiani, D., Fu, Y., Lu, J., Lin, Y*., et al.*
653 (2011). A resource of Cre driver lines for genetic targeting of GABAergic neurons in cerebral cortex.
654 Neuron *71*, 995-1013.
655 Vazquez, R., and Amat, P. (1978). The ultrastructure of the Herring bodies in rats subjected to
656 different experimental conditions. Cell Tissue Res *189*, 41-51.
657 Walker, L.C., Cornish, L.C., Lawrence, A.J., and Campbell, E.J. (2019). The effect of acute or
658 repeated stress on the corticotropin releasing factor system in the CRH-IRES-Cre mouse: A
659 validation study. Neuropharmacology *154*, 96-106.
660 Wamsteeker Cusulin, J.I., Fuzesi, T., Watts, A.G., and Bains, J.S. (2013). Characterization of
661 corticotropin-releasing hormone neurons in the paraventricular nucleus of the hypothalamus of
662 Crh-IRES-Cre mutant mice. PLoS One *8*, e64943.
663 Xiong, H., Zhou, Z., Zhu, M., Lv, X., Li, A., Li, S., Li, L., Yang, T., Wang, S., Yang, Z*., et al.* (2014).
664 Chemical reactivation of quenched fluorescent protein molecules enables resin-embedded
665 fluorescence microimaging. Nat Commun *5*, 3992.
666 Yamazaki, Y., Shimizu, K., Keino, H., and Mizutani, A. (1981). Myelinated herring bodies in the
667 posterior part of the median eminence of the mouse. Cell Tissue Res *219*, 209-211.
668 Yan, X.X., Baram, T.Z., Gerth, A., Schultz, L., and Ribak, C.E. (1998). Co-localization of corticotropin-
669 releasing hormone with glutamate decarboxylase and calcium-binding proteins in infant rat

neocortical interneurons. Exp Brain Res *123*, 334-340.
Yang, Z., Hu, B., Zhang, Y., Luo, Q., and Gong, H. (2013). Development of a plastic embedding method for large-volume and fluorescent-protein-expressing tissues. PLoS One *8*, e60877.
Zheng, T., Yang, Z., Li, A., Lv, X., Zhou, Z., Wang, X., Qi, X., Li, S., Luo, Q., Gong, H., *et al.* (2013). Visualization of brain circuits using two-photon fluorescence micro-optical sectioning tomography. Opt Express *21*, 9839-9850.

Figures

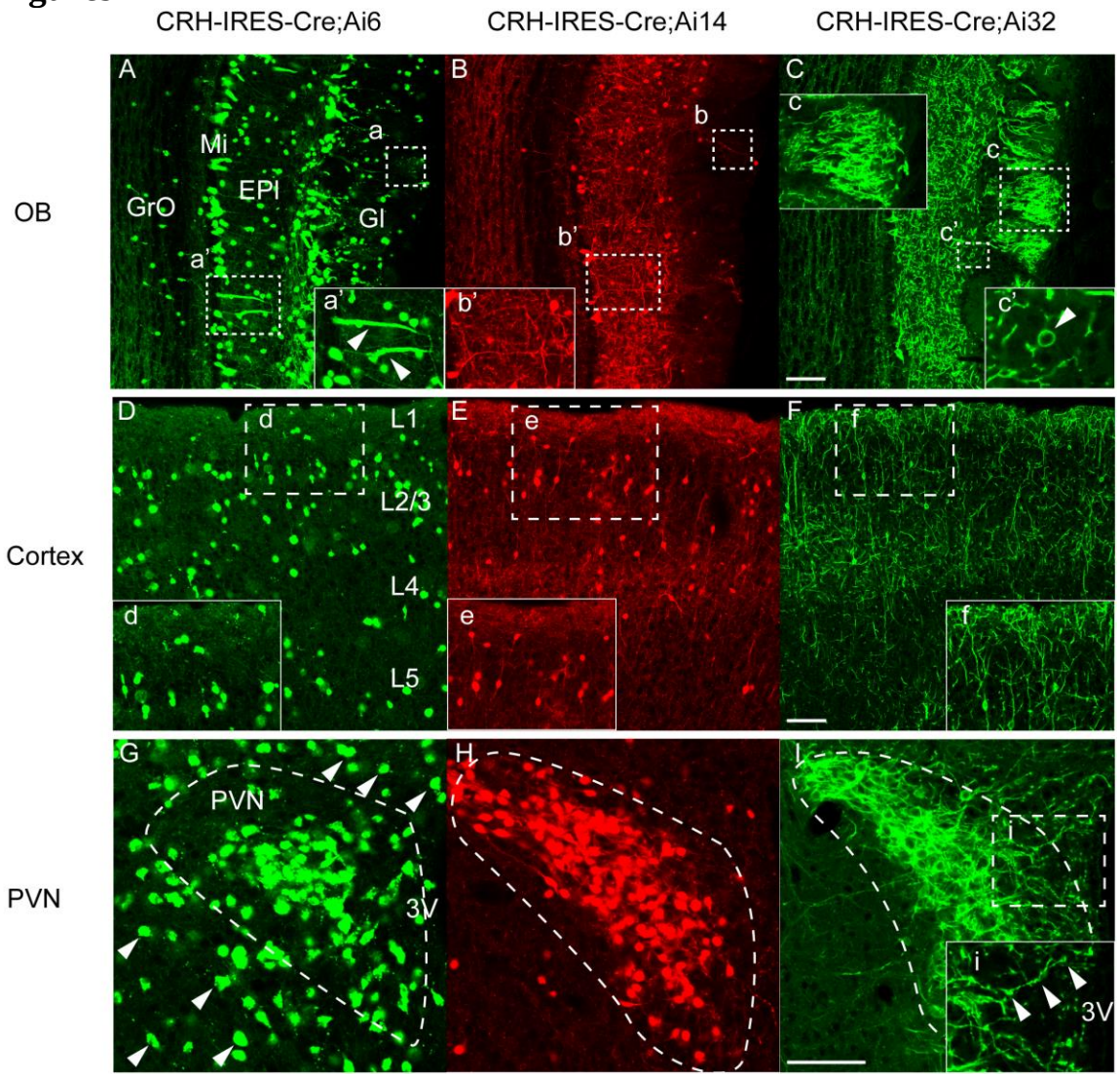

Figure 1. Comparison of the morphological features of CRH neurons in three fluorescent-reporter mouse lines.

Comparisons of the distributions and morphologies of fluorescent-labeled CRH neurons in several brain regions of CRH-IRES-Cre;Ai6, CRH-IRES-Cre;Ai14, and CRH-IRES-

683 Cre;Ai32 mice in the OB (A–C), cortex (D–F), and PVN (G–I). (A–C, a–c) The dotted
684 boxes show ZsGreen1 (a), td-Tomato (b) and EYFP (c) labeling of synaptic globular
685 structures in the Gl of the three mouse lines. (A–B, a'–b') The dotted boxes and magnified
686 images show ZsGreen1 (a') and td-Tomato (b') labeling of cell bodies and dendrites
687 (indicated by the arrowheads) in the Mi and EPl of CRH-IRES-Cre;Ai6 and CRH-IRES-
688 Cre;Ai14 mice. (C, c') The dotted box and magnified image show EYFP-labeled cell body
689 (indicated by the arrowhead) and dendrites in a CRH-IRES-Cre;Ai32 mouse. (D–F, d–f)
690 The dotted boxes and magnified images show ZsGreen1 (d), td-Tomato (e), and EYFP (f)
691 labeling of cell bodies and dendrites in layer 1 and layer 2/3 of the three mouse lines. (G)
692 ZsGreen1-labeled cell bodies in (dotted-curved box) and outside (arrowheads) of the PVN
693 of CRH-IRES-Cre;Ai6 mice. (H) Td-Tomato-labeled cell bodies in the PVN (dotted-
694 curved box) of CRH-IRES-Cre;Ai14 mice. (I and I, i) EYFP-labeled cells (I, dotted-curved
695 box) and fibers (i, dotted box and magnified image) in the PVN of CRH-IRES-Cre;Ai32
696 mice. Scale bars = 100 μm.
697

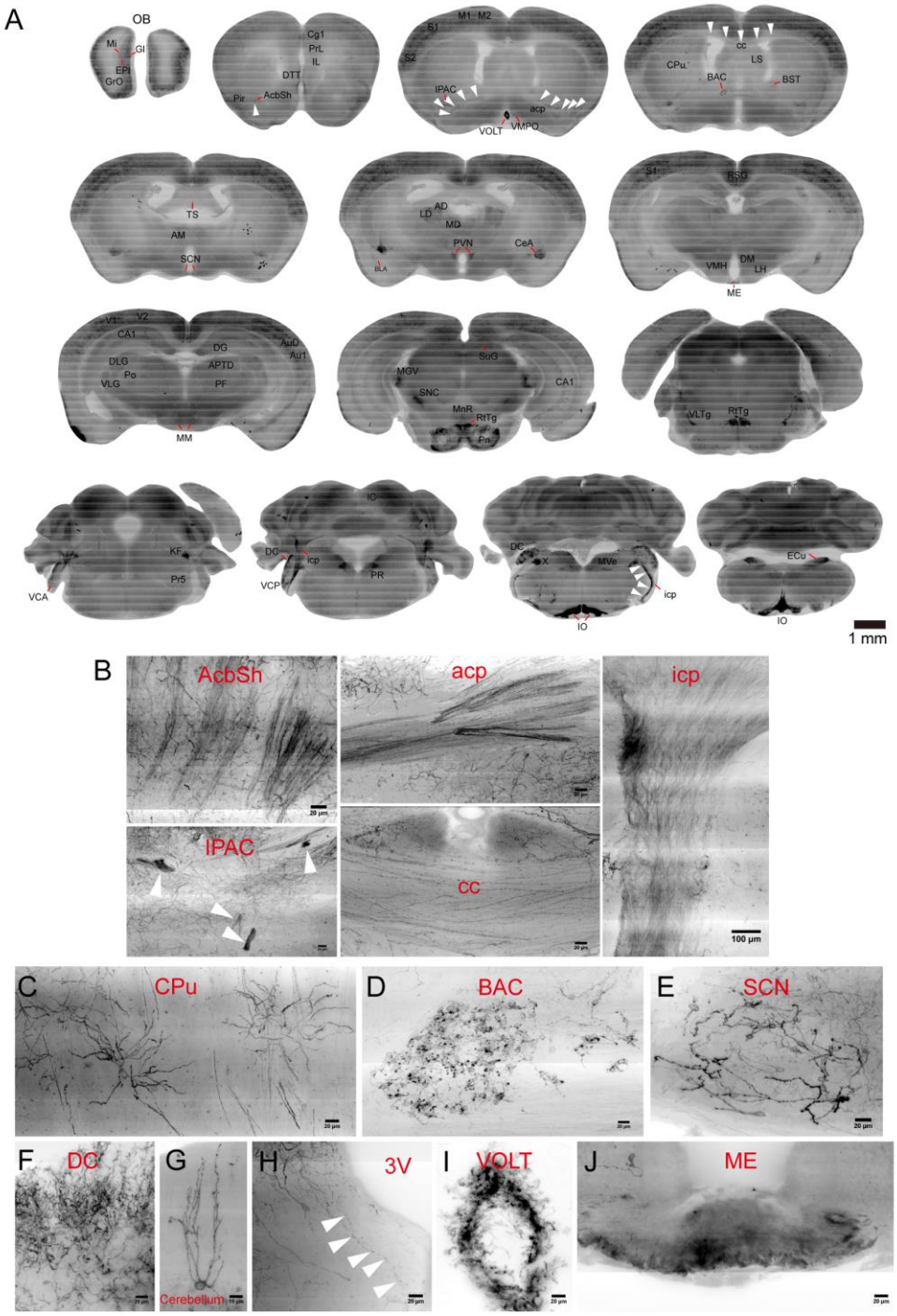

Figure 2. Whole-brain distributions of CRH neurons at high resolution in the CRH-IRES-Cre;Ai32 mouse line.

(A) Whole-brain distributions of EYFP-labeled CRH neurons, using the fMOST system, contained in 100-µm coronal-projected sections showing the general distributions of

704 EYFP-labeled CRH neurons in different brain regions. (B) EYFP-labeled clusters of fibers
705 projections from CRH neurons in the AcbSh, IPAC, acp, cc, and icp. (C) EYFP-labeled
706 single neurons in the CPu. (D) Clustered EYFP-labeled neurons distributed in the BAC.
707 (E) EYFP-labeled neurons in the SCN. (F) Dense EYFP-labeled dendrites from neurons in
708 the DC. (G) EYFP-labeled single neuron in the cerebellum. (H) EYFP-labeled fibers and
709 swollen structures around the 3V. (I) EYFP-labeled vascular like structures in the VOLT.
710 (J) EYFP-labeled terminals of PVN CRH neurons in the ME.

711

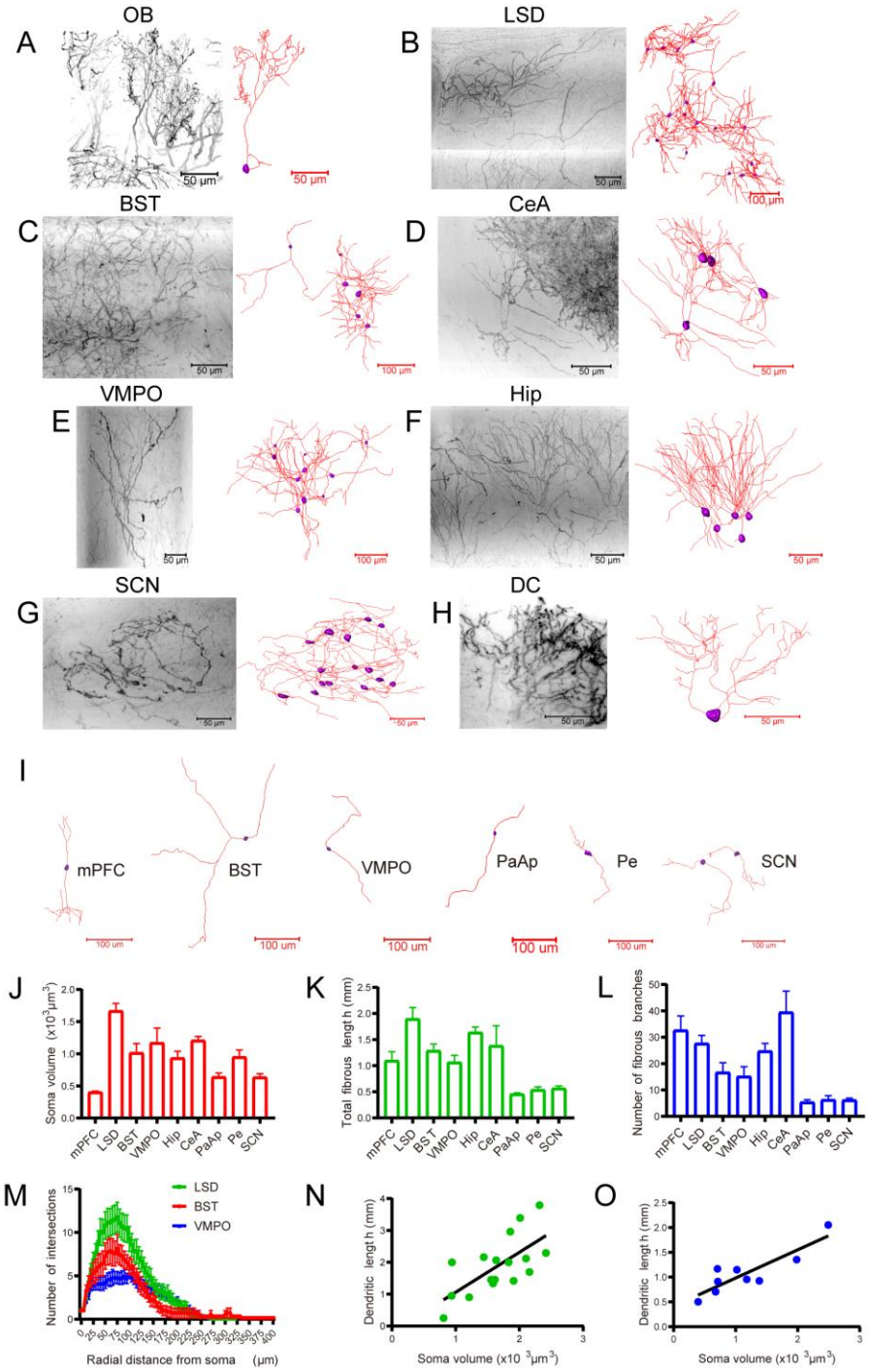

Figure 3. Three-dimensional distributions and single-cell reconstructions of CRH neurons in several brain regions.

(A–H) Original images (left half) and reconstructions (right half) of CRH neurons in different brain regions, including the OB (A), LSD (B), BNST (C), CeA (D), VMPO (E),

717 Hip (F), SCN (G), and DC (H). The original images were inverted into grayscale images.
718 The reconstructed somata and dendrites of neurons are indicated by purple bodies and red
719 lines, respectively. (I) Typical reconstructed neurons show the common bipolar
720 morphology found in different brain regions, including the mPFC, BNST, VMPO, PaAp,
721 Pe, and SCN. (J) Somatic volumes of CRH neurons in different brain regions [one-way
722 ANOVA, $P < 0.0001$, $F (8, 125) = 23.24$]. (K) Total fibrous lengths of CRH neurons in
723 different brain regions [one-way ANOVA, $P < 0.0001$, $F (8, 95) = 12.26$]. (L) Numbers of
724 fibrous branches of CRH neurons in different brain regions [one-way ANOVA, $P < 0.0001$,
725 $F (8, 101) = 11.53$]. (M) Sholl analysis of dendrites of neurons in the LSD, BNST, and
726 VMPO illustrate changes in the mean number of intersections with increasing radial
727 distance from the soma. (N) Correlation between dendritic length and somatic volume in
728 LSD neurons (Pearson's correlation coefficient $r = 0.68$, $P = 0.0029$). (O) Correlation
729 between dendritic length and somatic volume in VMPO neurons (Pearson's correlation
730 coefficient $r = 0.88$, $P = 0.0019$).
731

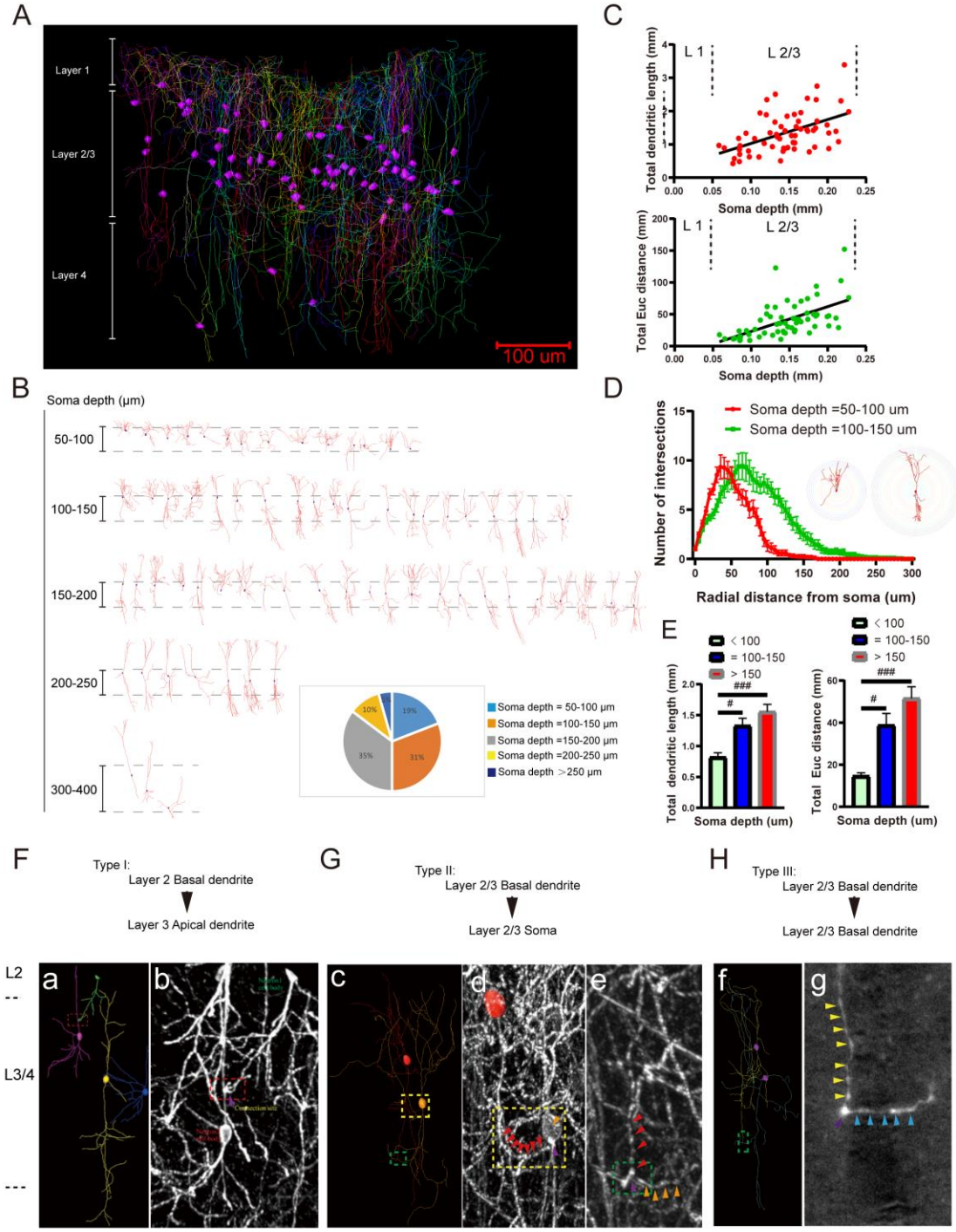

Figure 4. Multiple morphological types of CRH neurons form putative connections in the mPFC.

(A) Overview of reconstructed CRH neurons including somata (indicated by the purple bodies) and fibers (indicated by the colored lines) from layers 1–4 in a column with a

737 volume of 350 x 500 x 500 μm in a PrL subregion within the mPFC. (B) Representation of
738 67 reconstructed somata and dendrites of CRH neurons arranged along their somatic depths
739 with respect to the pial surface; the pie chart at the bottom right shows the percentages of
740 neurons distributed at different somatic depths. (C) Upper half: Correlation between total
741 dendritic length and somatic depth in PrL neurons (Pearson's correlation coefficient r =
742 0.51, P<0.0001); Lower half: Correlation between total Euclidean distance and somatic
743 depth in PrL neurons (Pearson's correlation coefficient r = 0.59, P<0.0001). (D) Sholl
744 analysis of the dendrites of neurons with somatic depths = 50–100 μm and 100–150 μm
745 illustrating changes in the mean number of intersections with increasing radial distance
746 from the soma; Inset images show exemplary intersections on two typical neurons (left:
747 somatic depth = 50–100 μm, right: somatic depth = 100–150 μm) with different somatic
748 depths. (E) Left: The total dendritic length of CRH neurons with somatic depths < 100 μm
749 showed differences compared with those with somatic depths = 100–150 μm (one-way
750 ANOVA, multiple comparisons, P = 0.0285) and soma depths >150 μm (one-way ANOVA,
751 multiple comparisons, P = 0.0005). Right: The total Euclidean distance of CRH neurons
752 with a somatic depth of < 100 μm showed differences compared with those with soma
753 depths = 100–150 μm (one-way ANOVA, multiple comparisons, P = 0.0213) and somatic
754 depths > 150 μm (one-way ANOVA, multiple comparisons, P = 0.0001). (F–H) Three types
755 of connections between CRH neurons in the mPFC. (F) a (reconstructed neurons) and b
756 (original image) show the type-I connection (the connection site is indicated by the purple
757 arrowhead in the red dotted box). (G) The yellow-dotted boxes in c (reconstructed neurons)
758 and d (original image) show the type-II connection (red arrowheads indicate a branch of
759 basal dendrites of one neuron and the orange arrowhead indicates the cell body of another
760 neuron; the connection site is indicated by the purple arrowhead). Green-dotted squares in
761 c (reconstructed neurons) and e (original image) showed the type-III connection (red
762 arrowheads indicated a branch of basal dendrites of one neuron and the orange arrowheads
763 indicate a branch of basal dendrites of another neuron; the connection site is indicated by
764 the purple arrowhead). (H) Green-dotted squares in f (reconstructed neurons) and g
765 (original image) also showed the type-III connection, (yellow arrowheads indicate a branch
766 of basal dendrites of one neuron and the blue arrowheads indicate a branch of basal

767 dendrites of another neuron; the connection site is indicated by the purple arrowhead).

768

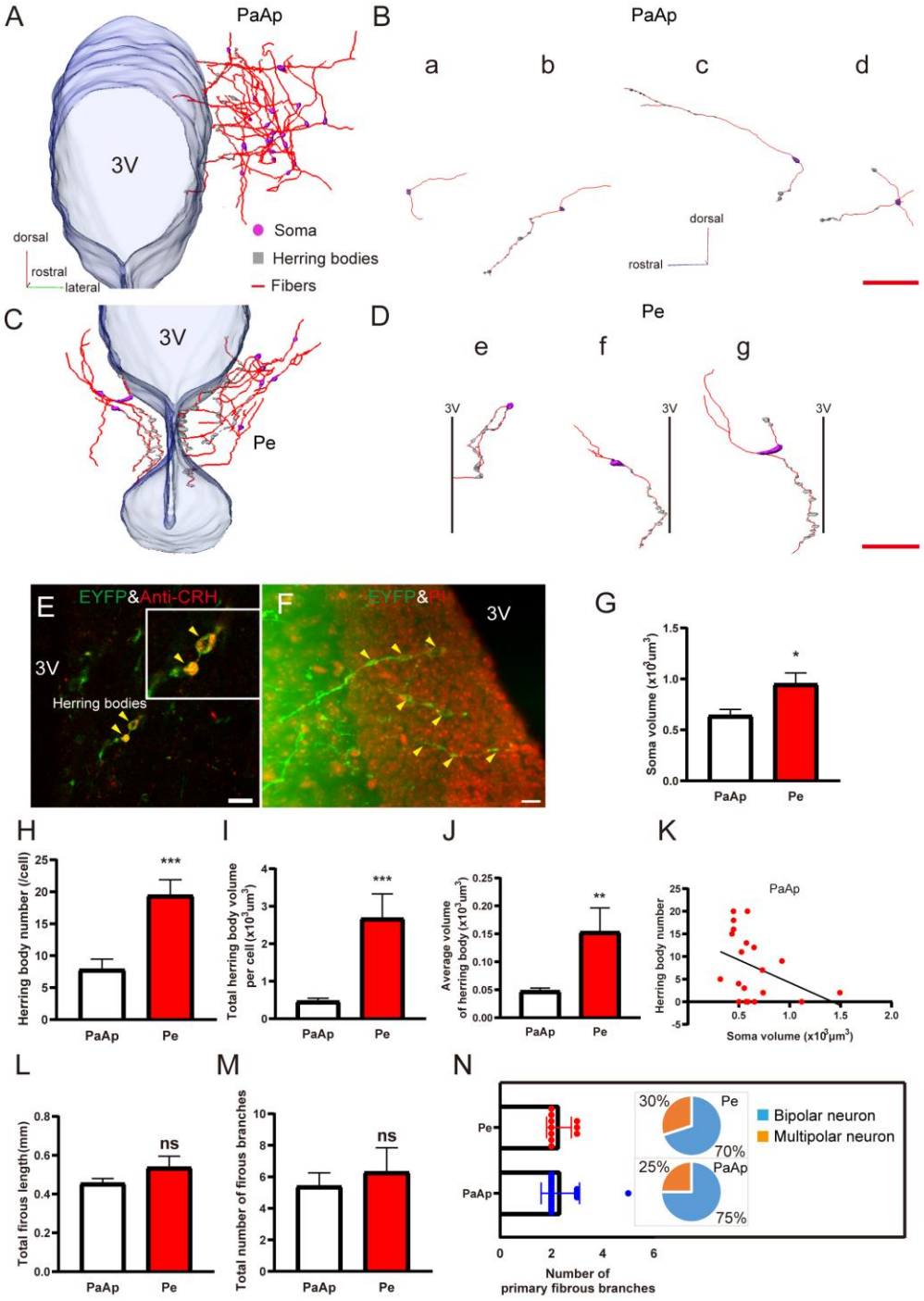

Figure 5. Reconstructions and morphological features of CRH Neurons in the PaAp and Pe.

(A) Three-dimensional distribution of reconstructed whole morphologies of CRH neurons in the PaAp. The somata are indicated by the purple bodies, the grey bodies indicate the

774 Herring bodies, and the red lines indicate the neural fibers; the transparent structure on the
775 left represents the reconstructed 3V. (B) Four typical reconstructed neurons in the PaAp.
776 B-a shows a bipolar neuron with short fibers and no Herring bodies; B-b shows a bipolar
777 neuron with Herring bodies located on the fiber at one end of the cell body. B-c shows a
778 bipolar neuron with Herring bodies located on fibers at both ends of the cell body; B-d
779 shows a multipolar neuron with Herring bodies located on the neural fibers (scale bar =
780 100 μm). (C) Three-dimensional distribution of reconstructed whole morphologies of CRH
781 neurons in the Pe. The somata are indicated by purple bodies, the grey bodies indicate the
782 Herring bodies, and the red lines indicate the fibers; the transparent structure in the center
783 represents the reconstructed 3V. (D) Three individual reconstructed neurons in the Pe. D-e
784 shows a bipolar neuron with both ends of fibers extending to the 3V and with Herring
785 bodies located on fibers at both ends of the cell body; D-f shows a bipolar neuron with one
786 end of the fiber extending to the 3V and with Herring bodies located on the fiber at one end
787 of the cell body; D-g show a multipolar neuron with one fiber extending to the 3V and with
788 Herring bodies mostly located on the fiber at one end of the cell body (scale bar = 100 μm).
789 (E) EYFP-labeled Herring bodies were CRH-antibody-positive (indicated by yellow
790 arrowheads, inset image is a magnified image). (F) The fiber ends with Herring bodies
791 located (indicated by yellow arrowheads) extended into the ependymal cell layer (indicated
792 by PI-stained cells) adjacent to the 3V. (G–J) Statistical results showing the differences of
793 somatic volume (G) ($P = 0.0119$), Herring body number (H) ($P = 0.0005$), total Herring
794 body volume per cell (I) ($P = 0.0003$), and the average volume of the Herring bodies (J) (P
795 $= 0.0047$) between neurons in the PaAp and Pe. (K) Correlation between somatic volume
796 and Herring-body-positive number of neurons in the PaAp. Spearman's correlation
797 coefficient was $r = -0.4519$, $P = 0.0455$. Each point in the scatterplot represents a single
798 cell. (L and M) There were no significant difference in fibrous features (L, total fibrous
799 length; M, total number of fibrous branches) of neurons between PaAp and Pe. ns: not
800 significant. (N) Comparison of primary fibrous branches and the proportions of bipolar or
801 multipolar cells in the PaAp and Pe.
802